ACS Catalysis

Research Article

pubs.acs.org/acscatalysis

Photocatalytic Water Oxidation by Hematite/Reduced Graphene Oxide Composites

Fanke Meng,[†] Jiangtian Li,[†] Scott K. Cushing,[‡] Joeseph Bright,[†] Mingjia Zhi,[†] Joseph D. Rowley,[‡] Zhanglian Hong,[§] Ayyakkannu Manivannan,[⊥] Alan D. Bristow,[‡] and Nianqiang Wu*[,†]

[†]Department of Mechanical and Aerospace Engineering and [‡]Department of Physics, West Virginia University, Morgantown, West Virginia 26506, United States

[§]State Key Laboratory of Silicon Materials, Department of Materials Science & Engineering, Zhejiang University, Hangzhou 310027, P.R. China

[⊥]National Energy Technology Laboratory, U.S. Department of Energy, Morgantown, West Virginia 26507, United States

Supporting Information

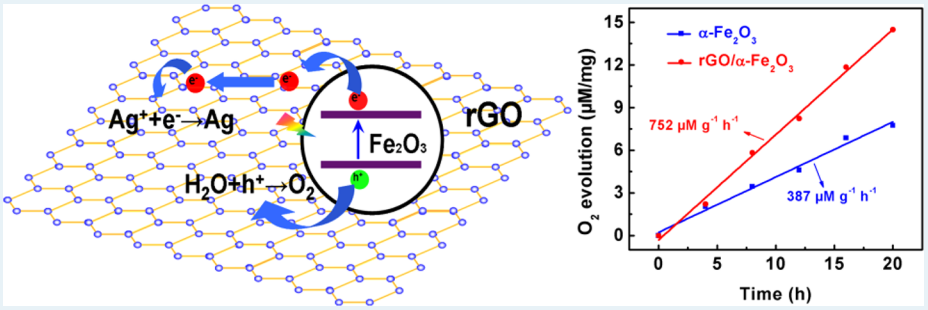

ABSTRACT: The photocatalytic water oxidation activity of hematite (α-Fe_2O_3) has been greatly enhanced by incorporating hematite nanoparticles on the reduced graphene oxide (rGO) nanosheets. Photoelectrochemical measurement results show that coupling the hematite nanoparticles with the rGO greatly increases the photocurrent and reduces the charge recombination rate. Transient absorption spectroscopy and time-domain terahertz spectroscopy have provided the direct evidence that the photogenerated electrons have transferred as the mobile carriers from α-Fe_2O_3 to rGO, which enhances the charge separation and suppresses the charge recombination. This work has provided new insight into the mechanism of photocatalysis enhancement by reduced graphene oxide, which has implications in the design of semiconductor/graphene heterojunction photocatalysts.

KEYWORDS: *photocatalyst, hematite, graphene, water splitting, transient absorption spectroscopy*

1. INTRODUCTION

Energy challenges have inspired the development of inexpensive and active materials for solar fuel production by photocatalytic water splitting.[1−3] Hematite (α-Fe_2O_3) stands out among many promising candidate materials because of its low cost and favorable band gap (2.1−2.2 eV) to absorb photons in the visible light range.[4,5] However, its photocatalytic efficiency is hindered by the short lifetime of the photogenerated charge carriers (<10 ps), short hole diffusion length (2−4 nm), and poor mobility of charge carriers (<0.2 $cm^2 \cdot V^{-1} \cdot s^{-1}$).[5,6] To address these limitations, α-Fe_2O_3 should be created as nanostructures to ensure that the charge carriers produced deep inside the α-Fe_2O_3 are able to diffuse to the hematite/electrolyte interface.[6,7] Many methods have been developed to engineer various morphologies of α-Fe_2O_3.[8,9] Nevertheless, α-Fe_2O_3 still suffers from a high charge recombination rate because of boundaries between the particles. α-Fe_2O_3 nanowires have shown the enhanced photoelectrochemical cell (PEC) performance[10,11] because one- or two-dimensional nanostructures generally have higher mobility and lower charge recombination rates than zero-dimensional nanoparticles.[12,13] However, the short hole diffusion length still limits the efficiency of charge carrier transport along the axial direction of the nanowires. Alternatively, α-Fe_2O_3 has been combined with charge-extraction layers to improve the charge separation by providing a more mobile hole pathway; the typical example being cobalt/phosphate catalyst or IrO_2 deposited onto α-Fe_2O_3 photoanodes.[4,14] Also, a *p-n* junction could effectively extract holes from α-Fe_2O_3 and improves the PEC performance.[2]

In contrast, coupling α-Fe_2O_3 with an electron acceptor is rare.[15] Graphene or reduced graphene oxide (rGO) are good candidates because of the high electron mobility (>15 000 $cm^2 \cdot V^{-1} \cdot s^{-1}$) and the flexible sheet nature that is beneficial to

Received: November 16, 2012
Revised: January 30, 2013
Published: March 4, 2013

support photocatalysts.[16] The previous studies have shown that the incorporation of graphene (or rGO) with metal oxide can enhance the photocatalytic activity.[15,16] It is claimed that photocatalysis enhancement by graphene is due to the fact that graphene provides a pathway for transport of charge carriers. However, no direct experimental evidence has yet been provided to prove this point. The graphene-enhanced photocatalysis mechanism remains poorly understood.

Herein, α-Fe_2O_3/rGO composites in which hematite nanoparticles are supported on the rGO nanosheets are synthesized by a hydrothermal process. The Fe_2O_3/rGO composite shows the enhanced photocatalytic activity toward water oxidation compared with the pristine α-Fe_2O_3 nanoparticles. Transient absorption and time-domain terahertz spectroscopy provide the direct evidence for the first time that electrons can transfer as the mobile carriers from α-Fe_2O_3 into the rGO, which can diffuse and become trapped, thus reducing the charge recombination rate.

2. EXPERIMENTAL METHODS

Materials Synthesis. Graphene oxide (GO) was synthesized by the established Hummer method.[17] The α-Fe_2O_3/reduced graphene oxide (rGO) was prepared by the hydrothermal method in a previous report.[18] Briefly, a proper amount of $FeCl_3{\cdot}6H_2O$ (97%, Alfa Aesar) was mixed with 44 mg of GO, and then the mixture was dissolved into 200 mL of deionized water (DI water, 18.2 MΩ·cm at 25 °C) and sonicated for 30 min. Then, 200 mL of ethanol (94−96%, Alfa Aesar) was mixed with the prepared solution and placed in a boiling aqueous bath for 2 h for thermal hydrolysis. Consequently, the α-Fe_2O_3/rGO sample was collected by centrifuging at a rate of 4000 rpm. Finally, the sample was heated in air at 350 °C for 2 h and then in pure nitrogen at 800 °C for 15 min. The α-Fe_2O_3/rGO ratio was adjusted by varying the amount of hematite precursor added during the hydrothermal process. Three ratios (1, 2, and 3 g of $FeCl_3{\cdot}6H_2O$) were employed in this study. According to the content of the rGO, the resulting samples were denoted as α-Fe_2O_3/rGO(h) with a high rGO content, α-Fe_2O_3/rGO with a medium rGO content, and α-Fe_2O_3/rGO(l) with a low rGO content, respectively. For preparation of monlithic α-Fe_2O_3, no GO was added into the solution, and the heating process was directly conducted in air at 800 °C for 15 min. A physical mixture of α-Fe_2O_3 and rGO (α-Fe_2O_3+rGO) was also prepared as a control sample to measure the photocatalytic water oxidation performance.

Characterizations and Light Absorption Measurement. The morphologies of α-Fe_2O_3 and α-Fe_2O_3/rGO were observed by a field-emission scanning electron microscope (SEM, JEOL 7600F) and a transmission electron microscope (TEM, JEOL JEM 2100F) respectively. For SEM sample preparation, 2 mg of powder sample was mixed in 1 mL of deionized water, which was then placed in an ultrasonic bath for 30 s to obtain a homogeneous suspension. Consequently, the suspension was deposited onto a precleaned silicon wafer substrate (1 cm ×1 cm, SPI Inc.), and then dried in air at 50 °C. For TEM sample preparation, the powder was suspended in ethanol and dropped onto a TEM grid (Ted Pella Inc.), and then dried at room temperature overnight. The crystal structures of α-Fe_2O_3 and α-Fe_2O_3/rGO were characterized by a high-resolution TEM (HRTEM) and X-ray diffraction (XRD, X′ Pert Pro PW3040-Pro, Panalytical Inc.) with Cu Kα radiation. X-ray photoelectron spectroscopy (XPS, PHI 5000 Versa Probe System, Physical Electronics, MN) was used for determining the chemical status of Fe and C. The C 1s peak at 284.6 eV worked as a reference to calibrate the binding energies in XPS spectra. Shimadzu 2550 UV−visible spectrometer equipped with an integrating sphere (UV 2401/2, Shimadzu) was used to obtain the UV−visible absorption spectra under the diffuse reflection mode. The typical sample preparation for the UV−visible spectrometer was pressing the sample powder (0.3−0.5 g) onto a pre-pressed $BaSO_4$ paste to form a solid pellet. The Fourier transform infrared spectra (FTIR) were obtained from the KBr pellet containing the α-Fe_2O_3 and the α-Fe_2O_3/rGO samples under transmission mode with a Nicolet 6700 spectrometer (Thermo Scientific, Waltham, MA). The surface areas of all the samples were measured by the Brunauer−Emmett−Teller (BET) method with the instrument of Micromeritics ASAP 2020. The content of rGO was measured by Thermogravimetric Analysis (TGA, TA Instrument Q50).

Photocatalytic Water Oxidation Testing. The simulated sunlight (light intensity: 80 mW/cm^2) was generated by a commercial xenon lamp solar simulator (300 W, Newport) equipped with an AM 1.5G filter. The α-Fe_2O_3 and α-Fe_2O_3/rGO samples were used for oxygen generation by photocatalytic water splitting as follows. First, DI water was boiled on a hot plate for 10 min to ensure all oxygen dissolved into the water was bubbled out. Second, the oxygen-free DI water and a magnetic stirring bar were added in a 100 mL quartz flask, which was then sealed with a septum stopper. Third, pure nitrogen was injected into the flask to squeeze out 85 mL of DI water. Fourth, 6 mg of the α-Fe_2O_3 or α-Fe_2O_3/rGO samples and 68 mg of $AgNO_3$ (>99%, Sigma-Aldrich) were mixed with 5 mL of the oxygen-free DI water and ultrasonicated for 30 s and then injected into the flask, so the total liquid in the flask was 20 mL. Fifth, the flask was then placed in an ultrasonic bath for another 10 min to form a homogeneous suspension. Sixth, the flask was exposed to the light for 4, 8, 12, 16, and 20 h, respectively. Finally, 5 mL of gas sample was extracted from the flask to measure the gas composition at each reaction time with a gas chromatograph (GC) equipped with a thermal conductivity detector (TCD).

The stability of the photocatalytic water oxidation was evaluated by measuring the rate of photocatalytic O_2 evolution in four cycles of the re-collected samples. Between each cycle, the photocatalyst was collected by centrifuging the suspension and then redissolved into 0.02 M $AgNO_3$ solution and sealed into a quartz flask. The detail procedure was identical as that described above.

Photoelectrochemical Measurement. First, 0.1 g of α-Fe_2O_3 or α-Fe_2O_3/rGO samples were mixed with 0.5 mL of terpineol (~95%, Sigma-Aldrich) and stirred on a magnetic stirrer for 24 h. Second, the terpineol suspension was coated onto fluorine-doped tin oxide (FTO) glass substrates (Hartford, TEC 15) with the doctor blading technique to prepare a series of photoelectrodes under the similar conditions to ensure the same thickness of each photoelectrode. Third, the α-Fe_2O_3 or α-Fe_2O_3/rGO photoelectrodes were dried on a hot plate and then transferred to a quartz tubular furnace to sinter in nitrogen at 550 °C for 2 h. Fourth, a silver wire was linked on the FTO with silver paste and then the epoxy was solidified onto the sample-uncovered areas on FTO substrate to avoid short current in the following electrochemical measurement.

Photoelectrochemical measurement was conducted with a three-electrode cell using the prepared photoanodes as the working electrode, Pt wire as the counter electrode, and Ag|

dx.doi.org/10.1021/cs300740e | ACS Catal. 2013, 3, 746−751

AgCl as the reference electrode. As the electrolyte, 1 mol/L NaOH (>98.0%, Sigma-Aldrich) aqueous solution (pH = 13.6) was bubbled for 30 min with N_2 prior to measurement. The identical light source used in the photocatalysis experiments was applied to illuminate the samples. The *J-V* curve was acquired with a Gamry electrochemical station (Reference 3000). The obtained potentials vs Ag|AgCl can be converted to the reversible hydrogen electrode (RHE) according to the following Nernst equation:

$$E_{RHE} = E + 0.05916pH + E_0 \quad (1)$$

Where E_{RHE} is the potential vs RHE, E_0 = 0.1976 V at 25 °C, and E is the measured potential vs Ag|AgCl.

Transient Absorption and Time Domain Terahertz Spectroscopy. The optical measurement was performed with a LIBRA one-box regenerative amplifier with 3.5 mJ of pulse energy at a repetition rate of 1 kHz. The 100 fs, 800 nm pulses were split into a frequency doubled pump pulse at 800 nm and an optical parametric amplifier, which allowed a tuning range of 550−2940 nm. Probe light was detected in a 30 cm Spex monochromator with a silicon photodetector (Vis-NIR) or using an InGaAs photodetector (IR). For Terahertz pump probe measurements the THz probe pulse was created by utilizing the 1200 nm output of the OPerA Solo to pump a ZGP crystal, creating a THz pulse from 0.5 to 3 THz. The THz pulse was collected, focused, and detected using a four off-axis parabolic mirror setup. The THz pulse was detected using electro-optic sampling in ZnTe. The decay of the peak of the THz pulse was monitored as a function of probe delay time to extract decay rates. Experiments were performed using a pump fluence of ~1 mJ/cm^2 for both THz and visible/infrared (IR) probes. Samples were dispersed in a KBr matrix. The KBr matrix transmits in the visible, IR and THz wavelength ranges. It was ensured that the matrix did not affect the recombination dynamics by comparing the signal for drop coated films and the KBr matrix. All samples were mass normalized and had similar static absorptions at the probe wavelengths used.

3. RESULTS AND DISCUSSIONS

Four types of samples were prepared by the hydrothermal processing and the follow-up heat treatment: (a) the α-Fe_2O_3/rGO(h) composites containing 6.1 wt % of reduced graphene oxide (rGO) as shown in Supporting Information, Figure S1, (b) the α-Fe_2O_3/rGO composites containing 3.8 wt % of rGO as shown in Figure 1, (c) the α-Fe_2O_3/rGO(l) composites containing 2.9 wt % of rGO as shown in Supporting Information, Figure S2, and (d) pristine α-Fe_2O_3 as shown in Supporting Information, Figure S3(a). The rGO contents in the α-Fe_2O_3/rGO composites were calculated from the TGA data in Supporting Information, Figure S4. It can be seen that the α-Fe_2O_3 sample showed a little loss in mass from room temperature to 200 °C, which was apparently due to the loss of adsorbed water. The α-Fe_2O_3/rGO composites containing different rGO contents demonstrated weight losses in the temperature ranges of 20−100 °C, 150−220 °C, and 420−550 °C, respectively, which corresponded to the losses of the adsorbed water, the residual groups on the rGO, and the burn-out of rGO, respectively.

SEM and TEM images in Figures 1a and 1b show the morphology of the α-Fe_2O_3/rGO composite. The particle sizes of α-Fe_2O_3 and α-Fe_2O_3/rGO increased after heating in N_2 (Supporting Information, Figure S3, Figure 1a, and Supporting Information, Figure S5). The TEM image of an α-Fe_2O_3 particle on the rGO sheet shows single-crystalline structure with a lattice spacing of 3.74 Å (Supporting Information, Figure S6), corresponding to the (012) plane (JCPDS: 33-0664). From the XRD patterns in Figure 1c, iron oxide in both samples was indexed as hematite. The crystalline sizes were calculated based on the strong diffraction peak (104) by using the Scherrer equation. The crystalline size of monlithic α-Fe_2O_3 (63.8 nm) was larger than that of α-Fe_2O_3 (41.4 nm) grown on the rGO sheets. The broad peak located at about 27° in α-Fe_2O_3/rGO was assigned to be rGO.[19] The UV−visible absorption spectra in Figure 1d shows an absorption edge at 600 nm, corresponding to the band gap of α-Fe_2O_3 at 2.07 eV. Absorption at wavelengths longer than 600 nm was much stronger in the composite structure because of the presence of rGO. Figure 1e shows the FTIR spectra of the α-Fe_2O_3/rGO composite. Signatures from the typical functional groups in the GO,[20] such as C═O (1736 cm^{-1}),[20−22] benzene ring skeletal vibration (1623 cm^{-1}),[20] aromatic C═C (1573 cm^{-1}),[20] COO^- (1404 cm^{-1}),[20,21] C−OH (1221 cm^{-1}),[20] C−O (1119 cm^{-1})[20] and C−O−C (1035 cm^{-1}),[20] were observed before heating. After heating, the intensities of C═O, COO, C−OH, C−O, and C−O−C band were reduced, but the benzene ring skeletal vibration signature remained, indicating that the GO was reduced. The XPS spectra of the C 1s core level in Figure 1f were deconvoluted into the sp^2 carbon (284.6 eV), C−O−C (285.6 eV), C−OH or α-C in −C−COOH (286.7 eV), C═O (288.0 eV) and COOH (289.1 eV), respectively.[20,23,24] The significant drops of the peaks at 285.6, 286.7, 288.0, and 289.1 eV indicated the reduction of GO. However, there was no change in the XPS spectra of Fe 2p of the α-Fe_2O_3 and the α-

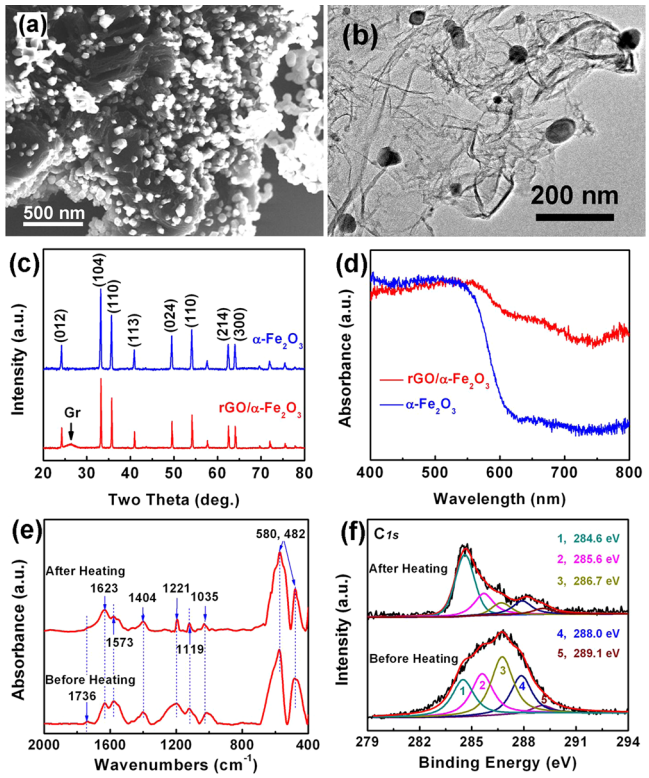

Figure 1. (a) SEM and (b) TEM images of the α-Fe_2O_3/rGO; (c) XRD patterns of the α-Fe_2O_3 and α-Fe_2O_3/rGO; (d) UV−visible absorption spectra of α-Fe_2O_3 and α-Fe_2O_3/rGO; (e) and (f) are FTIR spectra and XPS spectra of the α-Fe_2O_3/rGO before and after heating in N_2 at 800 °C.

dx.doi.org/10.1021/cs300740e | ACS Catal. 2013, 3, 746−751

Fe_2O_3/rGO in Supporting Information, Figure S7. The characterization data demonstrated that the α-Fe_2O_3/rGO composite was successfully formed. The specific surface areas were 19.3 m^2/g and 24.9 m^2/g for the pure α-Fe_2O_3 sample and the rGO/α-Fe_2O_3 composite, respectively.

Both the α-Fe_2O_3 and the α-Fe_2O_3/rGO were irradiated under simulated solar light to evaluate the photocatalytic activity toward oxygen evolution from water. As shown in Figure 2a, the O_2 generation rate was measured to be 387

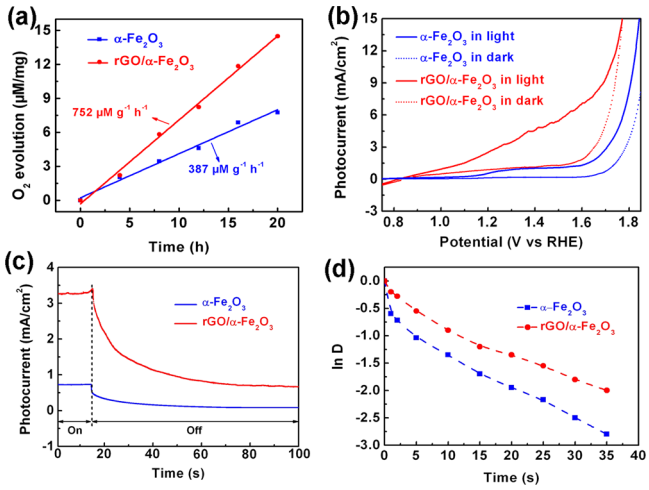

Figure 2. (a) Normalized O_2 evolution plots of the α-Fe_2O_3 and α-Fe_2O_3/rGO; (b) Photocurrent densities (J) as a function of the applied voltage (V vs RHE) of the α-Fe_2O_3 and α-Fe_2O_3/rGO with and without irradiation under AM 1.5G simulated solar light; (c) Photocurrent decay curves of the α-Fe_2O_3 and α-Fe_2O_3/rGO at the bias of 1.23 V vs RHE; (d) Normalized plots of the photocurrent–time dependence for the α-Fe_2O_3 and α-Fe_2O_3/rGO.

$\mu M \cdot g^{-1} \cdot h^{-1}$ for the α-Fe_2O_3 and 752 $\mu M \cdot g^{-1} \cdot h^{-1}$ for the α-Fe_2O_3/rGO composite, respectively. Normalized by surface area, the O_2 generation rates were 20.1 $\mu M \cdot m^{-2} \cdot h^{-1}$ for α-Fe_2O_3 and 30.2 $\mu M \cdot m^{-2} \cdot h^{-1}$ for the α-Fe_2O_3/rGO composite, respectively. Coupling a semiconductor with rGO is one of the effective routes to improve the photocatalytic activity of semiconductors.[25,26] In the present work, the α-Fe_2O_3/rGO composites with different rGO contents exhibited a difference in the photocatalytic activity toward oxygen evolution. A too high rGO content resulted in sparse α-Fe_2O_3 particles on the rGO sheets (Supporting Information, Figure S1). A too low rGO content led to the heavily agglomerated α-Fe_2O_3 particles on the rGO sheets (Supporting Information, Figure S2); and some of α-Fe_2O_3 particles were not supported on the rGO sheets. Consequently, both the α-Fe_2O_3/rGO(h) (Supporting Information, Figure S8c) and the α-Fe_2O_3/rGO(l) (Supporting Information, Figure S8b) exhibited worse photocatalytic activity than the α-Fe_2O_3/rGO with an optimal rGO content (Supporting Information, Figure S8a). In addition, a physical mixture of α-Fe_2O_3 with rGO was prepared as a control sample. This physical mixture (α-Fe_2O_3+rGO) in Supporting Information, Figure S8e showed much worse photocatalytic activity than the hydrothermally prepared α-Fe_2O_3/rGO composite (Supporting Information, Figure S8a) although both samples had the same rGO content (3.8 wt %). According to the average photocatalytic O_2 evolution rate measured with four cycles, the five samples showed the order: α-Fe_2O_3/rGO > α-Fe_2O_3/rGO(h) > α-Fe_2O_3 > α-Fe_2O_3/rGO(l) > α-Fe_2O_3+rGO. This indicated that the interaction of α-Fe_2O_3 with rGO played an important role in the photocatalytic activity.

To further understand why the α-Fe_2O_3/rGO composite showed better photocatalytic activity than the α-Fe_2O_3 alone, both the powder samples were immobilized on the FTO electrodes. Figure 2b shows the PEC behavior of both samples. The photocurrent observed in α-Fe_2O_3 started at 1.05 V vs RHE, rose to 0.80 mA cm^{-2} at 1.23 V vs RHE, and finally reached 1.30 mA cm^{-2} before the dark current onset. For the α-Fe_2O_3/rGO, the photocurrent onset shifted to lower potential (0.8 V vs RHE), and the photocurrent density increased continuously up to 6 mA cm^{-2} before the dark current onset. Small oscillation of photocurrent was observed at around 1.4 eV. A similar phenomenon was also shown in the previous literature.[27,28] The dark current for the α-Fe_2O_3/rGO indicated that some electrons were transferred from rGO to the electrode.[29] Two conclusions were drawn from the J-V curves. First, the lower onset potential of the α-Fe_2O_3/rGO indicates a smaller kinetic energy barrier for charge transfer across the interface of rGO and α-Fe_2O_3.[4,5] In other words, rGO can lower the overpotential required for water oxidation of α-Fe_2O_3. Second, the photocurrent of the α-Fe_2O_3/rGO composite (6 mA·cm^{-2}) was higher than the pristine α-Fe_2O_3 (1.0–3.0 mA·cm^{-2}), which was in agreement with the previous literature.[4,5] The higher photocurrent of the α-Fe_2O_3/rGO must be due to more electrons being transferred to the photoelectrode, which is only possible if rGO acted as an electron transfer channel, transferring the photogenerated electrons from α-Fe_2O_3.[29,30]

Electron transfer to the rGO could increase the charge separation and suppress the charge recombination, leaving long-lived holes in the α-Fe_2O_3 to oxidize water, increasing the photocatalytic water splitting rate. Transient photocurrent plots for α-Fe_2O_3 and α-Fe_2O_3/rGO photoelectrodes at a constant potential (1.23 V vs RHE) confirmed this scenario. After the potential was removed, the α-Fe_2O_3 revealed a sharper photocurrent drop off than the α-Fe_2O_3/rGO. The photocurrent of the rGO/α-Fe_2O_3 decayed to the dark current level slower than α-Fe_2O_3. To quantitatively determine the charge recombination behavior, a normalized parameter D is introduced: [31]

$$D = (I_t - I_{st})/(I_{in} - I_{st}) \quad (2)$$

where I_t, I_{st}, and I_{in} are the time-dependent, steady-state and initial photocurrents, respectively. Figure 2d shows the normalized plots of ln$D$–t. The transient time constant (τ) is defined as the time when ln$D$ = 1,[31] which reflects the general behavior of charge recombination. From Figure 2d, τ was estimated to be 4.8 s for α-Fe_2O_3 and 10.6 s for α-Fe_2O_3/rGO. The larger transient time constant for the composite structure indicates that it has a lower charge recombination rate than the α-Fe_2O_3 alone.

The mechanism for the enhanced photocatalytic activity toward water oxidation by α-Fe_2O_3/rGO was directly determined using transient absorption spectroscopy. Detailed background information regarding transient absorption is supplied in the Supporting Information. The decay of carriers photoexcited by a 400 nm excitation pulse was measured using both a broadband THz pulse[32] (0.5–3 THz) and a 700 nm visible light probe for the rGO, α-Fe_2O_3, and α-Fe_2O_3/rGO composite (Figure 3). The 700 nm probe is sensitive to trapped and mobile carriers, while the THz probe is only sensitive to mobile carriers since it has energy less than k_BT at room

dx.doi.org/10.1021/cs300740e | ACS Catal. 2013, 3, 746–751

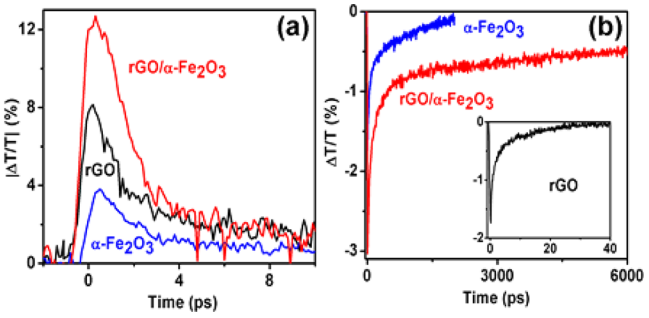

Figure 3. Transient absorption data for a 400 nm excitation pulse with (a) a THz probe, and (b) a 700 nm probe wavelength.

temperature.[33] The THz probe in Figure 3a shows that mobile carriers were created in the constituent α-Fe_2O_3 and rGO, then decayed on a picosecond time scale because of carrier trapping and coupling to acoustic and optical phonons.[34−36] The recombination dynamics in the α-Fe_2O_3/rGO composite showed a different behavior than its constituents, with a broadened initial peak which then underwent a two-stage decay process. The broadening indicated that mobile carriers were still being created well after the initial excitation pulse (~100 fs) and then decayed along the rGO recombination pathways. This was only possible if the mobile carriers created in the α-Fe_2O_3 were being transferred to the rGO within several picoseconds of the initial excitation.

The dynamics of the transferred carriers were determined using the 700 nm probe with the same excitation conditions as the THz probe. In general, the 700 nm probe is sensitive to mobile and trapped electrons. However, a 700 nm probe only corresponds to electron trap states in rGO.[34] The photoexcited carriers in α-Fe_2O_3 decayed within ~1 ns (Figure 3b). The photoexcited carriers in rGO decayed quickly because of the metallic like behavior of rGO, as shown in the inset in Figure 3b. The composite structure again differed from both the constituents. The composite structure had an electron trap state population with a decay time greater than 6 ns. This indicated that after injection of electrons into α-Fe_2O_3, they quickly diffused throughout the rGO and became trapped as long-lived carriers. The trap states were caused by the structural disorder and the oxygen-containing functional groups in rGO.[34]

The relative transmission $|\Delta T|/T$, which is proportional to the number of carriers created, was significantly larger for the composite than either of its constituents, indicating an increased charge separation rate. The increased separation rate was seen for the probe wavelengths well into the infrared region (Supporting Information, Figure S9). This suggested that the interface states between the rGO and α-Fe_2O_3 further contributed to charge separation, offering a possible explanation for the enhancement in the PEC at a low voltage. The differences in decay rate were due to diffusion of the photoinjected electrons into the rGO, and not due to change in the electronic structure of the composite, as proven by the probe wavelengths at the GO and −OH resonances (Supporting Information, Figure S9).

Transient absorption measurements proved the photocatalysis enhancement mechanism in the α-Fe_2O_3/rGO composite as illustrated in Scheme 1. In this scheme, mobile electrons are initially created in α-Fe_2O_3, quickly transfer to the rGO sheet, where they diffuse into trap states in the rGO on a time scale of picoseconds. These long-lived trapped electrons then react with the Ag^+, while the accumulated holes in the α-Fe_2O_3 lead to water oxidation, generating O_2. Alternatively, in a PEC, the trapped electrons can hop between successive layers of rGO to reach the photoelectrode, leading to an increase in the photocurrent and the recombination time. The interface of rGO and α-Fe_2O_3 enhances the charge separation rate, increasing the photocurrent.

Scheme 1. Schematic of Charge Transfer in the α-Fe_2O_3/rGO Composite

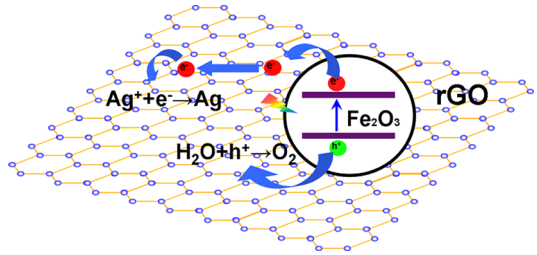

4. CONCLUSIONS

In summary, an α-Fe_2O_3/rGO composite was synthesized for photocatalytic water oxidation. The suppressed charge recombination and enhanced charge separation in α-Fe_2O_3 was due to extraction of the photogenerated electrons from α-Fe_2O_3 to rGO, which resulted in the enhanced photocatalytic activity toward oxygen evolution. This mechanistic study has paved a way for improving the photocatalytic activity of semiconductors with the poor charge mobility and the short charge carrier diffusion length.

■ ASSOCIATED CONTENT

Supporting Information

Further details about SEM, TEM, XPS, TGA characterizations, photocatalytic activity stability and transient absorption analysis are given in Figures S1−S9. This material is available free of charge via the Internet at http://pubs.acs.org.

■ AUTHOR INFORMATION

Corresponding Author

*Fax: +1-304-293-6689. Phone: +1-304-293-3326. E-mail: nick.wu@mail.wvu.edu.

Notes

The authors declare no competing financial interest.

■ ACKNOWLEDGMENTS

The resource and facilities used were partially supported by Research Challenge Grant from the State of West Virginia (EPS08-01), the West Virginia University Research Corporation, and the West Virginia EPSCoR Office. S.K.C. was supported by the National Science Foundation Graduate Research Fellowship (1102689). We are indebted to the West Virginia University Shared Facility. Z. H. is grateful to National Science Foundation of China (NSFC No. 51072180).

■ REFERENCES

(1) Meng, F. K.; Li, J. T.; Hong, Z. L.; Zhi, M. J.; Sakla, A.; Xiang, C. C.; Wu, N. Q. *Catal. Today* **2013**, *199*, 48.
(2) Li, J. T.; Meng, F. K.; Suri, S.; Ding, W. Q.; Huang, F. Q.; Wu, N. Q. *Chem. Commun.* **2012**, *48*, 8213.
(3) Cushing, S. K.; Li, J. T.; Meng, F. K.; Senty, T.; Suri, S.; Zhi, M. J.; Li, M.; Bristow, A.; Wu, N. Q. *J. Am. Chem. Soc.* **2012**, *134*, 15033.
(4) Tilley, S. D.; Cornuz, M.; Sivula, K.; Gratzel, M. *Angew. Chem., Int. Ed.* **2010**, *49*, 6405.

(5) Sivula, K.; Zboril, R.; Formal, F. L.; Robert, R.; Weidenkaff, A.; Tucek, J.; Frydrych, J.; Gratzel, M. *J. Am. Chem. Soc.* **2010**, *132*, 7436.
(6) Li, L.; Yu, Y. H.; Meng, F.; Tan, Y. Z.; Hamers, R. J.; Jin, S. *Nano Lett.* **2012**, *12*, 724.
(7) Townsend, T. K.; Sabio, E. M.; Browning, N. D.; Osterloh, F. E. *Energy Environ. Sci.* **2011**, *4*, 4270.
(8) Kay, A.; Cesar, I.; Gratzel, M. *J. Am. Chem. Soc.* **2006**, *128*, 15714.
(9) Cesar, I.; Kay, A.; Martinez, J. A. G.; Gratzel, M. *J. Am. Chem. Soc.* **2006**, *128*, 4582.
(10) Chernomordik, B. D.; Russell, H. B.; Cvelbar, U.; Jasinski, J. B.; Kumar, V.; Deutsch, T.; Sunkara, M. K. *Nanotechnology* **2012**, *23*, 194009.
(11) Mayer, M. T.; Du, C.; Wang, D. *J. Am. Chem. Soc.* **2012**, *134*, 12406.
(12) Wu, N. Q.; Wang, J.; Tafen, D. N.; Wang, H.; Zheng, G. Z.; Lewis, J. P.; Liu, X. G.; Leonard, S. S.; Manivannan, A. *J. Am. Chem. Soc.* **2010**, *132*, 6679.
(13) Meng, F. K.; Hong, Z. L.; Arndt, J.; Li, M.; Zhi, M. J.; Yang, F.; Wu, N. Q. *Nano Res.* **2012**, *5*, 213.
(14) Zhong, D. K.; Sun, J. W.; Inumaru, H.; Gamelin, D. R. *J. Am. Chem. Soc.* **2009**, *131*, 6086.
(15) Kim, J. Y.; Jang, J. W.; Youn, D. H.; Kim, J. Y.; Kim, E. S.; Lee, J. S. *RSC Adv.* **2012**, *2*, 9415.
(16) Lightcap, I. V.; Kosel, T. H.; Kamat, P. V. *Nano Lett.* **2010**, *10*, 577.
(17) Hummers, W. S.; Offeman, R. E. *J. Am. Chem. Soc.* **1958**, *80*, 1339.
(18) Song, H. J.; Jia, X. H.; Li, N.; Yang, X. F.; Tang, H. *J. Mater. Chem.* **2012**, *22*, 895.
(19) Li, N.; Liu, G.; Zhen, C.; Li, F.; Zhang, L. L.; Cheng, H. M. *Adv. Funct. Mater.* **2011**, *21*, 1717.
(20) Li, M.; Cushing, S. K.; Zhou, X.; Guo, S.; Wu, N. Q. *J. Mater. Chem.* **2012**, *22*, 23374.
(21) Wu, N. Q.; Fu, L.; Su, M.; Aslam, M.; Wong, K. C.; Dravid, V. P. *Nano Lett.* **2004**, *4*, 383.
(22) Lim, M. S.; Feng, F.; Chen, X. Q.; Wu, N. Q.; Raman, A.; Nightingale, J.; Gawalt, E. S.; Korakakis, D.; Hornak, L. A.; Timperman, A. T. *Langmuir* **2007**, *23*, 2444.
(23) Stankovich, S.; Piner, R. D.; Chen, X. Q.; Wu, N. Q.; Nguyen, S. T.; Ruoff, R. S. *J. Mater. Chem.* **2006**, *16*, 155.
(24) Tang, L. H.; Wang, Y.; Li, Y. M.; Feng, H. B.; Lu, J.; Li, J. H. *Adv. Funct. Mater.* **2009**, *19*, 2782.
(25) Xu, A. W.; Gao, Y.; Liu, H. Q. *J. Catal.* **2002**, *207*, 151.
(26) Wang, W. S.; Wang, D. H.; Qu, W. G.; Lu, L. Q.; Xu, A. W. *J. Phys. Chem. C.* **2012**, *116*, 19893.
(27) Frydrych, J.; Machala, L.; Tucek, J.; Siskova, K.; Filip, J.; Pechousek, J.; Safarova, K.; Vondracek, M.; Seo, J. H.; Schneeweiss, O.; Gratzel, M.; Sivula, K.; Zboril, R. *J. Mater. Chem.* **2012**, *22*, 23232.
(28) Chang, C. Y.; Wang, C. H.; Tseng, C. J.; Cheng, K. W.; Hourng, L. W.; Tsai, B. T. *Int. J. Hydrogen Energy* **2012**, *37*, 13616.
(29) Ng, Y. H.; Iwase, A.; Kudo, A.; Amal, R. *J. Phys. Chem. Lett.* **2010**, *1*, 2607.
(30) Jia, L.; Wang, D. H.; Huang, Y. X.; Xu, A. W.; Yu, H. Q. *J. Phys. Chem. C* **2011**, *115*, 11466.
(31) Tafalla, D.; Salvador, P.; Benito, R. M. *J. Electrochem. Soc.* **1990**, *137*, 1810.
(32) Rowley, J. D.; Pierce, J. K.; Brant, A. T.; Halliburton, L. E.; Giles, N. C.; Schunemann, P. G.; Bristow, A. D. *Opt. Lett.* **2012**, *37*, 788.
(33) Ulbricht, R.; Hendry, E.; Shan, J.; Heinz, T. F. *Rev. Mod. Phys.* **2011**, *3*, 543.
(34) Kaniyankandy, S.; Achary, S. N.; Rawalekar, S.; Ghosh, H. N. *J. Phys. Chem. C* **2011**, *115*, 19110.
(35) Joly, A. G.; Williams, J. R.; Chambers, S. A.; Xiong, G.; Hess, W. P. *J. Appl. Phys.* **2006**, *99*, 053521.
(36) Li, J. T.; Cushing, S. K.; Bright, J.; Meng, F. K.; Senty, T. R.; Zheng, P.; Bristow, A. D.; Wu, N. Q. *ACS Catal.* **2013**, *3*, 47.